RSC Advances

PAPER

View Article Online
View Journal | View Issue

Cite this: *RSC Adv.*, 2023, **13**, 2181

A hydrophilic carbon foam/molybdenum disulfide composite as a self-floating solar evaporator†

Ali Mohseni Ahangar,[a] Mohammad Ali Hedayati,[a] Mahdi Maleki,*[a]
Hajar Ghanbari,[a] Alireza Valanezhad[b] and Ikuya Watanabe[b]

Received 7th December 2022
Accepted 3rd January 2023

DOI: 10.1039/d2ra07810d

rsc.li/rsc-advances

Solar-driven interfacial evaporation has gained increasing attention as an emerging and sustainable technology for wastewater treatment and desalinization. The carbon/molybdenum disulfide (C/MoS_2) composite has attracted more attention due to its outstanding light absorption capability and optoelectronic properties as a solar steam generator. However, the hydrophobic nature of carbon and MoS_2-based materials hinders their wettability, which is crucial to the effective and facile operation of a solar generator of steam. Herein, a pH-controlled hydrothermal method was utilized to deposit a promising photothermal MoS_2 coating on melamine-derived carbon foams (CFs). The hydrophilic CF/MoS_2 composite, which can easily be floatable on the water surface, is a high-efficiency solar steam evaporator with a rapid increase in temperature under photon irradiation. Due to the localized heat confinement effect, the self-floating composite foam on the surface of water has the potential to produce a significant temperature differential. The porous structure effectively facilitates fast water vapor escape, leading to an impressively high evaporation efficiency of 94.5% under a light intensity of 1000 W m^{-2}.

1. Introduction

Despite the fact that more than 70% of the earth's surface is covered by water, only roughly 0.3% of our freshwater may be found in the surface water of lakes, rivers, and swamps. Four billion people are at risk due to the severe global crisis of freshwater shortage.[1] Fast industrialization, urbanization, and population growth have worsened these difficult worldwide problems.[2,3] Due to its capacity to collect and use readily available and limitless sunlight, solar-assisted water treatment, a type of desalination technology, has recently received widespread attention as a viable technique for very effective freshwater purification.[4] Due to its economical, non-polluting, and environmentally friendly functioning, this strategy has garnered a lot of interest. Water is a poor sunlight absorber, thus, photothermal materials capable of harvesting a wide range of light spectrum with solar energy-to-heat conversion ability can be utilized on the surface of the water.[5,6] For effective light absorption, a variety of photothermal materials have been used, such as carbon-based materials, plasmonic metal nanostructures, narrow band-gap semiconductors, polymers, and even rare materials.[7–11]

MoS_2 is a promising photothermal solar absorber for applications such as water evaporation due to its good features, including variable band-gap (1.3–1.9 eV), high carrier mobility, strong electron–hole confinement, and broad light absorption range from visible to near-infrared region. MoS_2 monolayers have been shown to have stronger sunlight absorption than the most popular solar absorbers, including GaAs, Si, and graphene, with a thickness of less than 1 nm and the ability to absorb 5–10% of the incident sunlight.[12,13] Owing to low cost, favorable thermal conductivity, black color, and high energy-conversion efficiency across the whole solar spectrum, carbon-based materials have been integrated with MoS_2 to operate as efficient solar steam generator composites.[14–20]

For very effective solar steam generation, a localized photothermal membrane made of an ultrathin flexible single-wall carbon nanotube (SWCNT)/MoS_2 composite film has been used. The prepared free-standing film displayed self-floating behavior and high light to thermal conversion efficiency, leading to an evaporative interface with the optimum temperature of 50 °C.[21] The onion-like graphene/MoS_2 hybrid aerogel beads have been proven for clean water production with a collection efficiency of ~21% under natural outside conditions on a typical spring day.[22] Nitrogen-doped graphene aerogel has been decorated by MoS_2 nanoflowers as a steam generator under low solar flux. Outstanding photothermal, water purification, and desalination performance were disclosed by the self-floating hybrid aerogel.[23]

---

[a] School of Metallurgy and Materials Engineering, Iran University of Science and Technology, Narmak, Tehran, 1684613114, Iran. E-mail: malekim@iust.ac.ir

[b] Department of Dental and Biomedical Materials Science, Graduate School of Biomedical Sciences, Nagasaki University, 1-7-1 Sakamoto, Nagasaki, 852-8588, Japan

† Electronic supplementary information (ESI) available. See DOI: https://doi.org/10.1039/d2ra07810d

A straightforward chemical reduction technique has been used to create a three dimensional (3D) porous photothermal graphene/MoS_2 composite hydrogel in which MoS_2 nanoflowers have been intercalated between the graphene layers. The hierarchically porous hydrogel in this proposed generator contributed to light trapping to enhance solar absorption, generated more dispersed hotspots to access and activate water.[24] Additionally, MoS_2 nanosheets were hydrothermally produced on low-temperature carbonized wood to make a solar steam generator. The prepared composite displayed about 96% solar absorption and a water evaporation rate of 1.49 kg m^{-2} h^{-1} under 1000 W m^{-2} simulated solar irradiation.[25] A robust composite with a significant evaporation area was produced by combining activated carbon fiber cloth and MoS_2 with a 3D hollow cone shape.[26] It is important to note that surface wettability is a key factor in water transport and affects the stability of solar evaporators. In general, the hydrophilic nature of solar absorbers persuades water transport to evaporate.[27,28] A new configuration of evaporator layers has been developed, consisting of a hydrophobic top layer and a hydrophilic bottom layer to simultaneously take advantage of two wetting states, in order to use hydrophobic materials as solar steam generators.[27] Herein, a solar steam evaporator made of a hydrophilic CF/MoS_2 composite was shown to be capable of easily floating on the water's surface. MoS_2 nanosheets were deposited on the CF made from commercial melamine foam using the pH-controlled hydrothermal technique to create a self-floating hydrophilic solar absorber composite. The prepared composite displayed an excellent evaporation rate of 1.43 kg m^{-2} h^{-1} with an high efficiency of 94.5% under one sun.

2. Experimental

2.1. Materials

Commercially available melamine foams (MFs) were provided by a domestic producer. Sodium molybdate (99.5%), sulfur powder (99%), and NaOH (99.8%) were purchased from Merck Co. (Darmstadt, Germany).

2.2. Composite synthesis

The MFs were pyrolyzed at 800 °C in a N_2 environment for one hour to produce CFs. Then, using a hydrothermal technique, MoS_2 nanosheets were applied to the ready CFs. In a nutshell, 60 cm^3 of deionized water was magnetically agitated for 30 minutes while 1.5 mmol $Na_2MoO_4 \cdot 2H_2O$ and 6 mmol sulphur powder were added. A piece of prepared CF was dipped into the resulting suspension and then brought to the autoclave. In both neutral (pH = 7, CMN sample) and basic (pH = 11, CMB sample) conditions, the hydrothermal treatment was conducted at 240 °C for 12 hours. NaOH was introduced to the reaction environment to set up the basic conditions. The obtained composites were dried at 70 °C after being repeatedly washed with ethanol and deionized water.

2.3. Solar-assisted evaporation

Solar-assisted evaporation tests have been carried out by simulated solar illumination at a constant intensity of 800, 1000, 1200, and 1400 W m^{-2}. A thermocouple coupled to a data logger module was used to measure temperature changes as a result of sun irradiation. The setup also included a balance to measure the mass of the water and a solar steam generation system (Fig. 1). The produced composites were used as an active photothermal material floating in the water, with a surface area of 3 cm^2 and thicknesses of 5 and 10 mm. The sample was dried at 60 °C in between each cycle of irradiation, which lasted 30 minutes. All solar evaporation experiments were tested at temperature of 26–28 °C and 50–55% humidity.

2.4. Characterization

SEM micrographs of the cross-section of the composite foam were acquired using a TESCAN VEGA/XMU microscope (Czech). The infrared spectra of powders were obtained by a Shimadzu 8400S Spectrometer (Japan) with a 4 cm^{-1} spectral resolution. Compressed KB pellets mixed with prepared powder were used to produce all spectra in the 500–4000 cm^{-1} range. XRD patterns were recorded using a diffractometer with Cu K_α (λ = 1.54 Å) radiation (X'Pert Pro MPD, Philips, Germany). A 532 nm laser was used as the excitation source for the Raman spectroscopy, which was carried out on a Takram micro Raman spectrometer (TeksanTM, Iran) with a power output of 90 mW and a spectral resolution of 6 cm^{-1}. A KRATOS Axis Ultra system was used to conduct the XPS measurements. The apparatus is equipped with a charge neutralization system, an aspherical mirror electron analyzer, and a monochromatized Al K X-ray source. The carbonaceous Au 4f line (84.2 eV) was used as the reference to calibrate the binding energies. A T-type thermocouple inserted in the test sample was attached to a data logger module (Advantech USB-4718) to collect the test temperature fluctuations, while an infrared camera (Ti27, Fluke, USA) recorded the temperature of composite.

3. Results

The SEM micrographs of MF and carbonized-MF at 800 °C are shown in Fig. 2(a) and (b), respectively. As can be seen, the resulting flexible CF maintained the initial melamine framework's 3D interconnected porous structure. In contrast to polymeric foam, the pores of CF appear to have shrinkage during the pyrolysis.

To prepare the composites, MoS_2 was deposited on the CFs *via* a one-step hydrothermal reaction at 240 °C under the different pHs of 7 and 11. By using XRD analysis, the crystalline structure of produced CF/MoS_2 composites were identified. Fig. 3(a) displays the XRD patterns of the CMN and CMB. CMN composite displays a peak around 14° as a characteristic peak of the hexagonal phase (2H) of MoS_2 assigned to (002) lattice fringes. Further, the appeared peaks at 33.4°, 39.9°, and 59.1° are attributed to (100), (103), and (110) reflections of the 2H-MoS_2 phase (JCPDS card no. 75-1539), respectively.[29] A broad peak about 25° that corresponded to CF as the composite

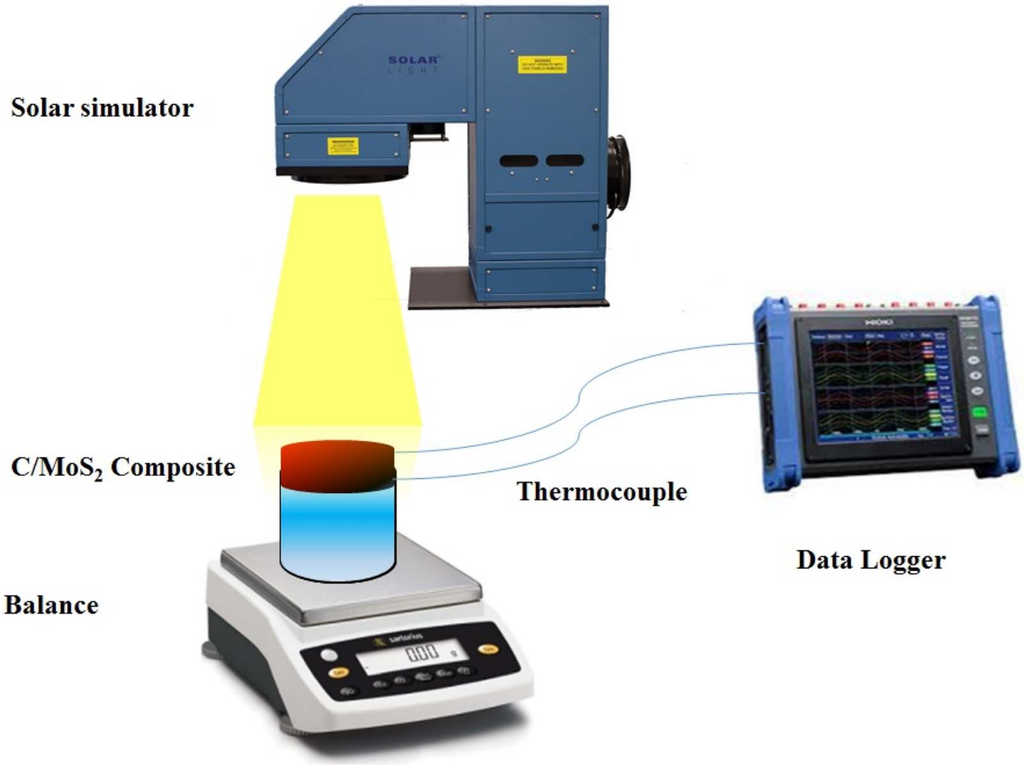

Fig. 1 Scheme of the set-up consisted of a solar simulator, a balance to record the water mass, and a thermocouple connected to a data logger to acquire the temperature variations during light irradiation.

framework also appeared in addition to MoS_2 diffraction peaks.[25] The growth of MoS_2 crystallographic planes was affected when the hydrothermal synthesis environment was switched from a neutral to a basic one. A comparison of CMN and CMB XRD patterns reveals that after basic synthesis, the relative intensity ratio of the (002) to (110) crystallographic peaks dropped. Because of layered structure of MoS_2 flowers, (002) diffraction has a higher intensity than other crystallographic planes, and it represents the favored orientation for growth.[30,31] This implies that basic issues may impede growth in this direction.

To assess the thickness of the MoS_2 nanosheets seen in Fig. 3(b) and to learn more about the bonding properties of the as-prepared nanocomposites, their Raman spectra were collected. The Raman spectrum of CMN composite shows MoS_2 characteristic peaks at about 380 cm^{-1} and 400 cm^{-1}, respectively, corresponding to the in-plane E^1_{2g} and out-of-plane A_{1g} mode of typical lamellar MoS_2 structure. CMB shows the weaker

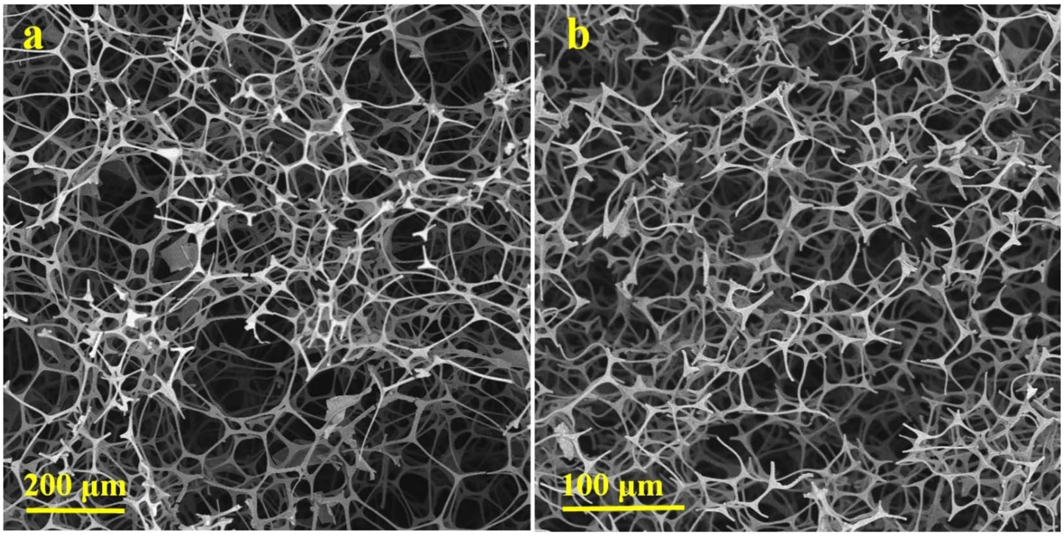

Fig. 2 SEM micrographs of (a) MF and (b) carbonized MF at 800 °C.

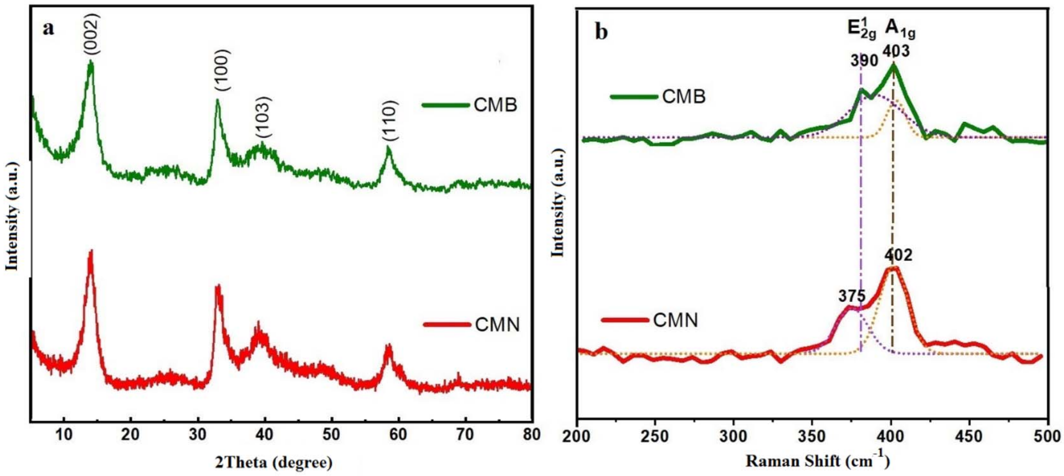

Fig. 3 (a) XRD patterns and (b) Raman spectra of CMN, and CMB samples.

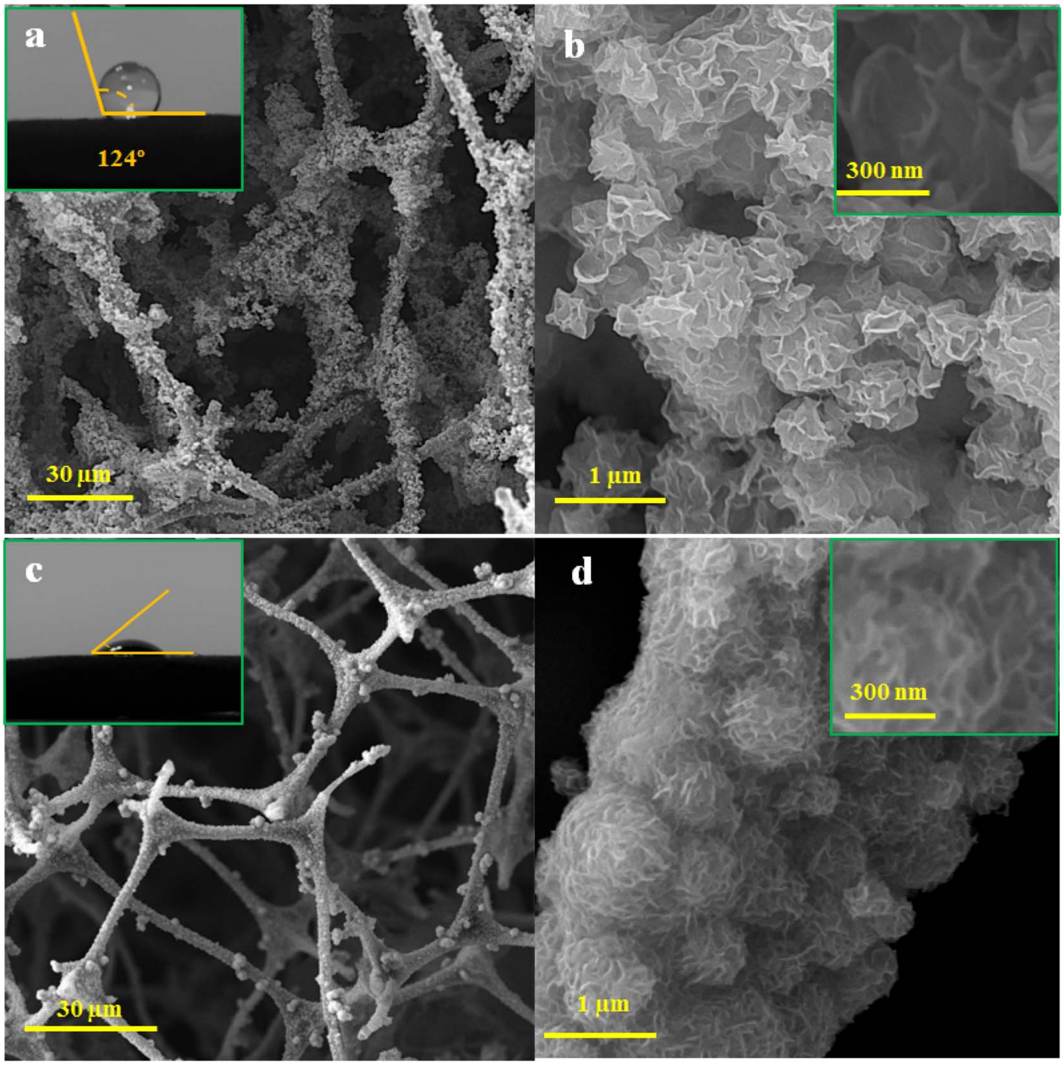

Fig. 4 SEM images of (a) and (b) CMN, and (c) and (d) CMB samples. The insets show wetting angles measured in (a) CMN, and (c) CMB samples in the case of a water droplet placed on the composite surface.

and wider E^1_{2g} mode in comparison to Raman spectra of the composite generated under neutral circumstances. The relatively broader E^1_{2g} peak with weaker intensity suggests that the crystal structure of MoS_2 may contain substantial defect sites.[32,33] However, Moe *et al.*,[34] noted that there was a pause between the Raman out-of-plane mode A_{1g} and the in-plane mode E^1_{2g} to specify the number of MoS_2 layers. When a basic solution is used, the measured $\Delta\omega$ reduced from 27 cm^{-1} to 13 cm^{-1} in CMB, which may indicate an apparent decrease in the number of layers.

Investigating the deposited MoS_2 shape on CFs under various synthesis conditions has been done using SEM images. The flower-like MoS_2 microspheres with sizes of about 1 ± 0.4 μm may be seen on CFs filaments for the CMN composite, as shown in Fig. 4(a) and (b). Nanosheets with a thickness of 50 ± 10 nm can be found in every flower-shaped microsphere of CMN, whereas they are thinner (30 ± 10 nm) in the CMB sample (Fig. 4(c) and (d)). In comparison to CMN composite, the SEM micrograph of CMB shows thinner MoS_2 layers and smaller distributed microspheres on the carbon framework, which is consistent with Raman spectrum investigations. It can also be supported by a wider (002) peak in the XRD of CMB compared to CMN, showing that the basic solution produced thinner nanosheets. This observation supports the XRD patterns of the produced composites appeared diffraction intensity variation, which indicated the orientational growth and smaller crystallite sizes.

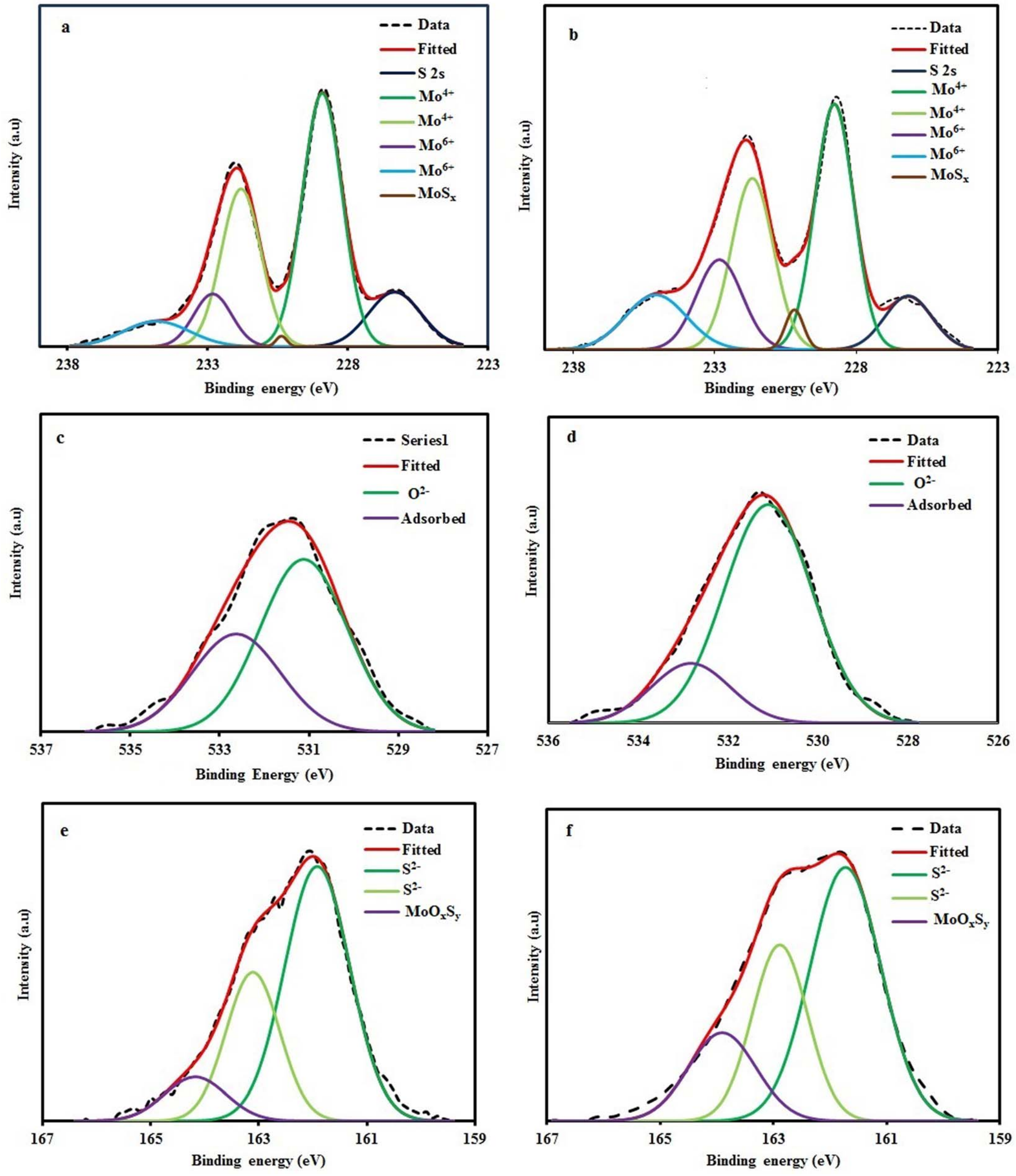

Fig. 5 High-resolution XPS spectra and peak positions of (a) Mo 3d (CMN), (b) Mo 3d (CMB), (c) O 1s (CMN), (d) O 1s (CMB), (e) S 2p (CMN), and (f) S 2p (CMB).

The spreading of a water droplet on the CF/MoS_2 nanocomposites was measured. The water droplets maintained a roughly spherical shape on the CMN nanocomposite surface with an approximate contact angle of 124°, confirming the superhydrophobic behavior, as seen in the wetting condition of the surface in the inset of Fig. 4(a). However, the hydrophilic behavior was detected by the wetting angle measurement in the samples made under standard circumstance, CMB. These hydrophilic foams are capable of floating unimpeded on the surface of water (Inset of Fig. 4(c) and S1†).

XPS analysis was used to assess the surface composition of the CMN and CMB composites. The Mo 3d XPS spectra of the composites are shown in Fig. 5(a) and (b), together with the accompanying deconvoluted Lorentzian–Gaussian peaks that were generated using the Shirley baseline correction approach. Five components with binding energies of 226.3, 228.9, 230.3, 231.8, 232.8, and 234.8 eV were identified in the deconvoluted Mo 3d XPS spectra of the CMN. The 228.9 and 232.82 eV peaks are attributed to the Mo $3d_{5/2}$ and $3d_{3/2}$, respectively, indicating bonding between Mo^{4+} and S^{2-} in 2H-MoS_2. The peak at 226.3 eV is assigned to the binding energy of S 2s electrons.[35,36] The doublet peaks at 231.3 and 234.8 eV provide evidence of low amounts of Mo^{6+}.[37] The MoS_x compounds may be the cause of the minor peak at 230.3 eV.[38] Similar Mo $3d_{5/2}$ and $3d_{3/2}$ peaks were seen in the CMB, proving that MoS_2 was successfully formed on CF. However, compared to the prepared sample under neutral conditions, the percentage of Mo^{6+} in CMB was increased. The surface chemistry and MoS_2 affinity to wettability were reported to change as a result of surface functionalizing bulk MoS_2 sheets. The hydrophilicity of the MoS_2 products was caused by the oxidation of the active edge sites in MoS_2 and anionic molybdates like MoO_x (which contain Mo^{6+}).[39]

On the other hand, the O 1s core level spectra of the composites were deconvoluted into two peaks (Fig. 5(c) and (d)). The O (−2) oxidation state is represented by the first peak at 531.1 eV, while the adsorbed species from the environment are responsible for the second peak at 532.6 eV.[40] Comparing the O 1s spectra of the produced composites reveals that the CMB sample has a greater oxygen content related to oxidation. Three peaks measured at 161.9, 163.1, and 164.1 eV were obtained from the deconvoluted S 2p signals in Fig. 5(e) and (f). The peaks of 161.9 and 163.1 eV are attributed to MoS_2 formation. At the same time, the peak at higher binding energy has been assigned to the involvement of oxygen in the MoO_xS_y formation. When the oxygen percent rises in MoO_xS_y compounds, the increasing of the high bonding energy region has been observed.[36,41] Therefore, the basic circumstance resulted in a higher oxygen content compared to the neutral condition.

The effectiveness of MoS_2 formation and growth on the wetting behavior of CMB led researchers to use an IR camera to examine how the material responded to light irradiation in terms of temperature (Fig. 6). As can be seen, rapid temperature increase to 50 °C caused by light illumination led to color change of the nanocomposite, quickly. Due to the carbon framework coated with MoS_2 nanoflowers with strong light absorption capacity and the subsequent high optical energy conversion into thermal energy, the surface temperature of the nanocomposite is rapidly rising. Even though the temperature of pure water is much lower than its evaporation temperature, locally generated heat on the surface might be the primary source of water evaporation.[42,43]

A suitable candidate for solar evaporation systems can be constructed by integrating strong hydrophilicity, acceptable floatability, and excellent light absorption of the composite. A piece of CMB composite with a thickness of 5 mm was floated on the water's surface in order to evaluate the effectiveness of solar evaporation. The temperature fluctuations of the CMB composite are shown in Fig. 7(a) when the light intensity is 800 W m^{-2}. As can be observed, the nanocomposite temperature increased monotonically over the period of 30 minutes to reach 41 °C, but the temperature diagram of pure water indicates a maximum temperature of 33.5 °C under the same circumstances. Furthermore, there was a 10 °C temperature difference between the area above and below the composite. This apparent temperature difference between the bulk water and the composite shows low heat conduction to the bulk water, while the composite has a significant heat absorption.[25] To consider the evaporator thickness, a composite with thicknesses of 5 mm was employed. When compared to the thinner composite, the composite with a 10 mm thickness reached a greater temperature and, as a result, had a higher water evaporation efficiency (Fig. 7(a)). For instance, the temperature of the thicker composite increased to 66 °C with the intensity of 1400 W m^{-2}, while the temperature of the thinner composite was 61 °C. The thicker photothermal absorber produced a better thermal barrier, which stopped heat from transferring to the water. The highest temperature increased to 48, 54, and

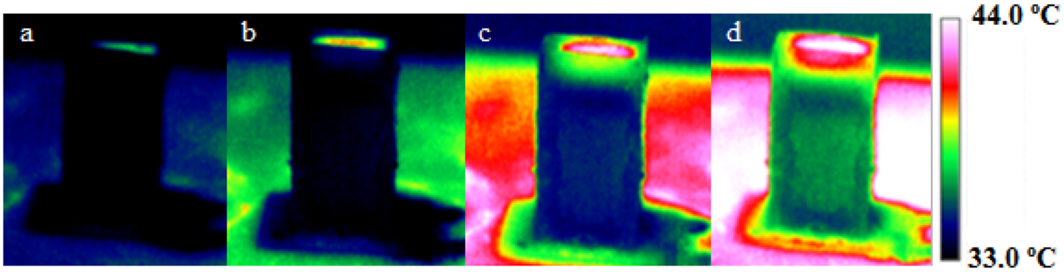

Fig. 6 Infrared images of CMB sample as the temperature response under light irradiation with an intensity of 1400 W m^{-2} after (a) 30 s, (b) 90 s, (c) 180 s and (d) 270 s.

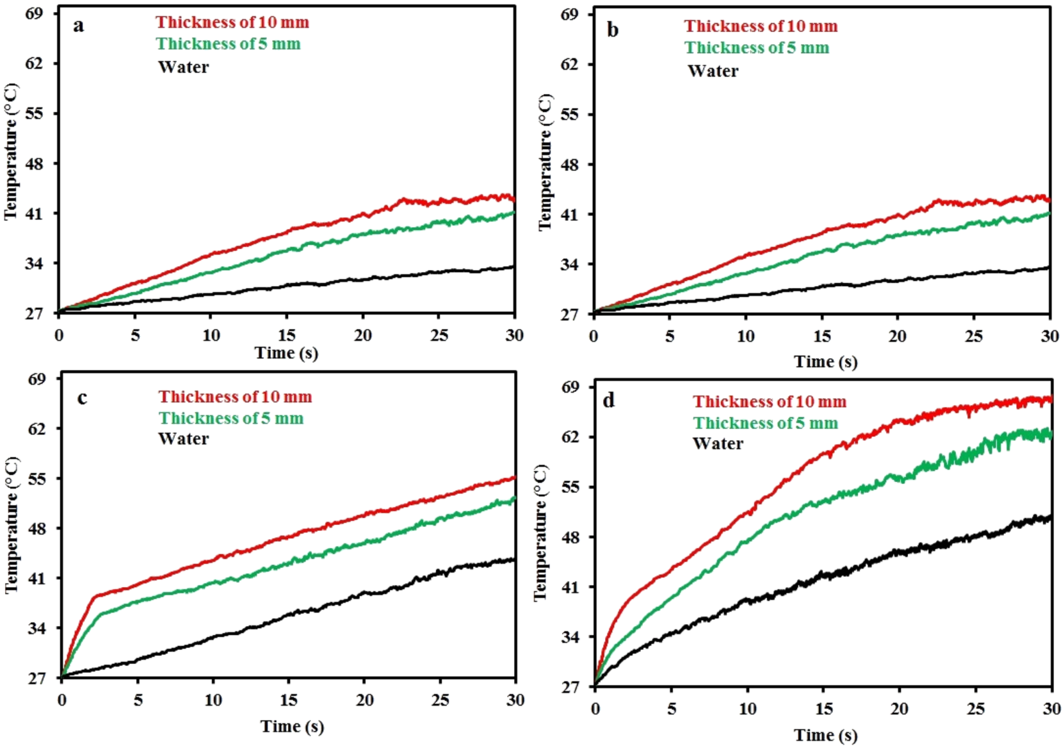

Fig. 7 Temperature changes with time under the light illumination for water and CMB foam with 5 and 10 mm thickness under the light intensity of (a) 800, (b) 1000, (c) 1200, and (d) 1400 W m^{-2}.

66 °C, respectively, when the light intensity was increased to 1000, 1200, and 1400 W m^{-2} in Fig. 7, demonstrating a direct relationship between the temperature observed and the applied light intensity. We need to thoroughly research the sun-to-vapor efficiency (η) in order to create a more effective solar steam generator:

$$\eta = \frac{\Delta H_{\text{vap}} r_{\text{water}}}{I_{\text{in}}} \tag{1}$$

where the ΔH_{vap} is the enthalpy of the liquid–vapor phase change, r_{water} is the evaporation rate, and I_{in} refers to the power density of solar irradiation on the absorber surface.[44] According to eqn (1), under the illumination of 800, 1000, 1200, and 1400 W m^{-2}, respectively, pure water evaporation without photothermal elements was calculated to be approximately 16.8, 17.1, 17.3, and 17.6 percent. Under light irradiation of 1000 W m^{-2}, this composite as a photothermal absorber revealed remarkable efficiency of 94.5 percent.

The next phase involved analyzing the mass variations of evaporated water and their rate with time. In Fig. 8, it was examined how the weight changes caused by water evaporation for CF/MoS$_2$ nanocomposite under light irradiation for 30 min at various light intensities. Under light intensities of 800, 1000, 1200, and 1400 W m^{-2}, respectively, the amounts of water that evaporated were 1.19, 1.43, and 1.73, and 2.21 kg m^{-2}. For comparison, the rate of pure water evaporation under the same conditions is measured, and it is found to be 0.2, 0.23, 0.27, and 0.33 kg m^{-2} at light intensities of 800, 1000, 1200, and 1400 W m^{-2}, respectively. As can be seen, the produced CF/MoS$_2$ composite greatly increases the evaporation rate.

The researchers used various carbon-based materials and molybdenum disulfide nanosheets to produce the C/MoS$_2$ composites, which are used as solar steam generators. Due to the efficient localized heat confinement, the single-wall CNT/MoS$_2$ film floating on the water surface could provide a sharp temperature gradient and high evaporation efficiency.[21] Under 1000 W m^{-2} of light intensity, MoS$_2$/bio-CF composites with a 10 mm thickness demonstrated an evaporation rate of 1.2 kg

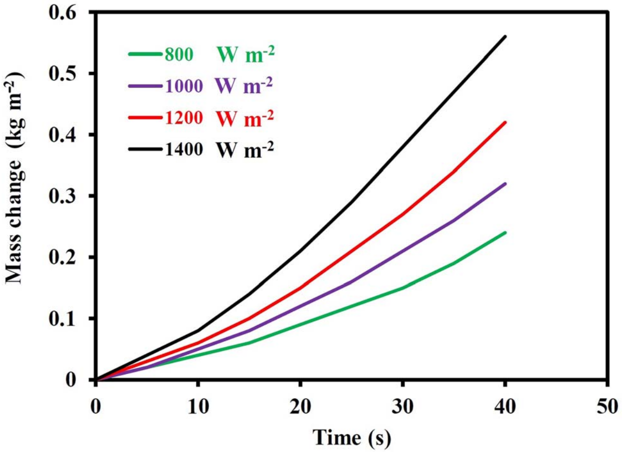

Fig. 8 Mass changes with time for CMB with 10 mm thickness under the light intensities of 800, 1000, 1200, and 1400 W m^{-2}.

m^{-2} h^{-1}.[25] A free-standing water reservoir with a high energy efficiency of 88 percent is made of C/MoS_2 microbeads electrostatically grown on a 3D polyurethane sponge.[20] The excellent evaporation efficiency of the produced composite may result from strong light absorption capacity of the MoS_2 nanosheets. Because of the well-distributed MoS_2 nanosheets on the surface of CF and the nanocrystalline size of the MoS_2 flower-like structure, the internal electronic vibrations provide a rough surface with high light reflectivity.[8]

4. Conclusion

In conclusion, we developed a facile method for fabricating a superhydrophilic and flexible solar steam generator. The MoS_2 nanosheets are successfully deposited on CF with improved evaporation rates, utilizing a straightforward pH-controlled hydrothermal process. The produced composites showed an effective solar-thermal conversion efficiency of 79.7, 81.4, 83.2 percent to 84.7 percent, respectively, under 800, 1000, 1200, and 1400 W m^{-2} of the sunshine. This was due to their good photothermal conversion, insulation, and quick water transfer. This module can be improved to produce drinking water and desalinate water in an environmentally friendly manner.

Conflicts of interest

There are no conflicts to declare.

References

1 J. Yin, *et al.*, Boron nanosheets loaded with MoS_2 porous sponges for water purification, *J. Water Process. Eng.*, 2021, **41**, 102048.

2 P. Tao, *et al.*, Solar-driven interfacial evaporation, *Nat. Energy*, 2018, **3**(12), 1031–1041.

3 C. Cai, *et al.*, Biomimetic 3D Membranes with MXene Heterostructures for Superior Solar Steam Generation, Water Treatment, and Electricity Generation, *Sol. RRL*, 2021, 2100593.

4 N. S. Lewis, Research opportunities to advance solar energy utilization, *Science*, 2016, **351**(6271), 353.

5 Y. Kuang, *et al.*, A high-performance self-regenerating solar evaporator for continuous water desalination, *Adv. Mater.*, 2019, **31**(23), 1900498.

6 Z. Guo, *et al.*, Achieving steam and electrical power from solar energy by MoS_2-based composites, *Chem. Eng. J.*, 2022, **427**, 131008.

7 R. Li, *et al.*, MXene Ti_3C_2: an effective 2D light-to-heat conversion material, *ACS Nano*, 2017, **11**(4), 3752–3759.

8 Z. Guo, *et al.*, PEGylated self-growth MoS_2 on a cotton cloth substrate for high-efficiency solar energy utilization, *ACS Appl. Mater. Interfaces*, 2018, **10**(29), 24583–24589.

9 K. Sun, *et al.*, Constructing of 3D porous composite materials of NiAl/CNTs for highly efficient solar steam generation, *Sol. Energy Mater. Sol. Cells*, 2022, **240**, 111722.

10 L. Gao, *et al.*, Two-dimensional metamaterials as metafoams for optimized surface-enhanced solar steam generation, *Sol. Energy Mater. Sol. Cells*, 2022, **243**, 111793.

11 W. Li, *et al.*, Portable Low-Pressure Solar Steaming-Collection Unisystem with Polypyrrole Origamis, *Adv. Mater.*, 2019, **31**(29), 1900720.

12 M.-L. Tsai, *et al.*, Monolayer MoS_2 Heterojunction Solar Cells, *ACS Nano*, 2014, **8**(8), 8317–8322.

13 M. Bernardi, M. Palummo and J. C. Grossman, Extraordinary Sunlight Absorption and One Nanometer Thick Photovoltaics Using Two-Dimensional Monolayer Materials, *Nano Lett.*, 2013, **13**(8), 3664–3670.

14 P. Cao, *et al.*, Gradient Heating Effect Modulated by Hydrophobic/Hydrophilic Carbon Nanotube Network Structures for Ultrafast Solar Steam Generation, *ACS Appl. Mater. Interfaces*, 2021, **13**(16), 19109–19116.

15 K. Xu, *et al.*, Architecting a Janus biomass carbon/sponge evaporator with salt-rejection and ease of floatation for sustainable solar-driven desalination, *Environ. Sci.: Water Res. Technol.*, 2021, **7**(5), 879–885.

16 W. Fang, *et al.*, Carbonized rice husk foam constructed by surfactant foaming method for solar steam generation, *Renewable Energy*, 2020, **151**, 1067–1075.

17 X. Zhang, *et al.*, MoS_2@C nanosphere as near infrared/pH dual response platform for chemical photothermal combination treatment, *Colloids Surf., B*, 2020, **192**, 111054.

18 H. Wang, *et al.*, Integrative treatment of anti-tumor/bone repair by combination of MoS_2 nanosheets with 3D printed bioactive borosilicate glass scaffolds, *Chem. Eng. J.*, 2020, **396**, 125081.

19 D. Han, *et al.*, Eco-friendly Hybrids of Carbon Quantum Dots Modified MoS_2 for Rapid Microbial Inactivation by Strengthened Photocatalysis, *ACS Sustainable Chem. Eng.*, 2020, **8**(1), 534–542.

20 W. Li, *et al.*, Synergistic High-Rate Solar Steaming and Mercury Removal with MoS_2/C @ Polyurethane Composite Sponges, *Adv. Energy Mater.*, 2018, **8**(32), 1802108.

21 X. Yang, *et al.*, An Ultrathin Flexible 2D Membrane Based on Single-Walled Nanotube–MoS_2 Hybrid Film for High-Performance Solar Steam Generation, *Adv. Funct. Mater.*, 2018, **28**(3), 1704505.

22 X. Feng, *et al.*, Novel onion-like graphene aerogel beads for efficient solar vapor generation under non-concentrated illumination, *J. Mater. Chem. A*, 2019, **7**(9), 4400–4407.

23 T. Lan, *et al.*, N-Doped Graphene Aerogels Decorated by MoS_2 Nanoflowers for Steam Generation under Low Solar Flux, *ACS Appl. Nano Mater.*, 2022, **5**(8), 10237–10247.

24 Y. Li, *et al.*, Composite hydrogel-based photothermal self-pumping system with salt and bacteria resistance for super-efficient solar-powered water evaporation, *Desalination*, 2021, **515**, 115192.

25 X. Zhang, G. Wu and X.-C. Yang, MoS_2 Nanosheet–Carbon Foam Composites for Solar Steam Generation, *ACS Appl. Nano Mater.*, 2020, **3**(10), 9706–9714.

26 E. Yang, *et al.*, Three-Dimensional Artificial Transpiration Structure Based on 1T/2H–MoS_2/Activated Carbon Fiber

Cloth for Solar Steam Generation, *ACS Appl. Mater. Interfaces*, 2022, **14**(26), 29788–29796.

27 Z. Qin, *et al.*, Bioinspired Hydrophilic–Hydrophobic Janus Composites for Highly Efficient Solar Steam Generation, *ACS Appl. Mater. Interfaces*, 2021, **13**(16), 19467–19475.

28 I. Ibrahim, *et al.*, Biomass-based photothermal materials for interfacial solar steam generation: a review, *Mater. Today Energy*, 2021, **21**, 100716.

29 K. K. Paul, *et al.*, Solar light driven photoelectrocatalytic hydrogen evolution and dye degradation by metal-free few-layer MoS_2 nanoflower/TiO_2(B) nanobelts heterostructure, *Sol. Energy Mater. Sol. Cells*, 2018, **185**, 364–374.

30 S. Zhang, *et al.*, Constructing Highly Oriented Configuration by Few-Layer MoS_2: Toward High-Performance Lithium-Ion Batteries and Hydrogen Evolution Reactions, *ACS Nano*, 2015, **9**(12), 12464–12472.

31 N. Islam, *et al.*, Fast supercapacitors based on vertically oriented MoS_2 nanosheets on plasma pyrolyzed cellulose filter paper, *J. Power Sources*, 2018, **400**, 277–283.

32 Z. Wu, *et al.*, Enhanced hydrogen evolution catalysis from osmotically swollen ammoniated MoS_2, *J. Mater. Chem. A*, 2015, **3**(24), 13050–13056.

33 K.-K. Liu, *et al.*, Growth of Large-Area and Highly Crystalline MoS_2 Thin Layers on Insulating Substrates, *Nano Lett.*, 2012, **12**(3), 1538–1544.

34 Y. A. Moe, *et al.*, Probing Evolution of Local Strain at MoS_2-Metal Boundaries by Surface-Enhanced Raman Scattering, *ACS Appl. Mater. Interfaces*, 2018, **10**(46), 40246–40254.

35 H. W. Wang, P. Skeldon and G. E. Thompson, XPS studies of MoS_2 formation from ammonium tetrathiomolybdate solutions, *Surf. Coat. Technol.*, 1997, **91**(3), 200–207.

36 N. M. D. Brown, N. Cui and A. McKinley, An XPS study of the surface modification of natural MoS_2 following treatment in an RF-oxygen plasma, *Appl. Surf. Sci.*, 1998, **134**(1), 11–21.

37 Y. Hu, *et al.*, Monolayer hydrophilic MoS_2 with strong charge trapping for atomically thin neuromorphic vision systems, *Mater. Horiz.*, 2020, **7**(12), 3316–3324.

38 P. Kumar, M. Singh and G. B. Reddy, Oxidized Core–Shell MoO_2–MoS_2 Nanostructured Thin Films for Hydrogen Evolution, *ACS Appl. Nano Mater.*, 2020, **3**(1), 711–723.

39 X. Yin, *et al.*, Surface functionalization of bulk MoS_2 sheets for efficient liquid phase exfoliation in polar micromolecular solvents, *Appl. Surf. Sci.*, 2019, **486**, 362–370.

40 S. Singh, *et al.*, MoS_2/MoO_2 Nanocomposite for Selective NH3 Detection in a Humid Environment, *ACS Sustainable Chem. Eng.*, 2021, **9**(21), 7328–7340.

41 B. Wang, *et al.*, MoS_x Quantum Dot-Modified Black Silicon for Highly Efficient Photoelectrochemical Hydrogen Evolution, *ACS Sustainable Chem. Eng.*, 2019, **7**(21), 17598–17605.

42 Y. Lin, *et al.*, Solar steam generation based on the photothermal effect: from designs to applications, and beyond, *J. Mater. Chem. A*, 2019, **7**(33), 19203–19227.

43 R. Xu, *et al.*, Construction of hierarchical 2D/2D Ti3C2/MoS_2 nanocomposites for high-efficiency solar steam generation, *J. Colloid Interface Sci.*, 2021, **584**, 125–133.

44 W. Li, *et al.*, Synergistic High-Rate Solar Steaming and Mercury Removal with MoS_2/C@ Polyurethane Composite Sponges, *Adv. Energy Mater.*, 2018, **8**(32), 1802108.